Acta Oceanol. Sin., 2022, Vol. 41, No. 5, P. 78–89
https://doi.org/10.1007/s13131-021-1878-z
http://www.aosocean.com
E-mail: ocean2@hyxb.org.cn

Dynamics of seasonal and interannual variability of the ocean bottom pressure in the Southern Ocean

Xiaoqin Xiong[1], Xuhua Cheng[1, 2*], Niansen Ou[3], Tao Feng[1, 2], Jianhuang Qin[1], Xiao Chen[1, 2], Rui Xin Huang[4]

[1] College of Oceanography, Hohai University, Nanjing 210024, China

[2] Southern Marine Science and Engineering Guangdong Laboratory (Zhuhai), Zhuhai 519080, China

[3] College of Ocean and Meteorology, Guangdong Ocean University, Zhanjiang 524088, China

[4] Woods Hole Oceanographic Institution, Woods Hole, MA 02543, USA

Received 6 April 2021; accepted 8 June 2021

Abstract

Seasonal and interannual variability of ocean bottom pressure (OBP) in the Southern Ocean was investigated using Gravity Recovery and Climate Experiment (GRACE) data and a Pressure Coordinate Ocean Model (PCOM) based on mass conservation. By comparing OBP, steric sea level, and sea level, it is found that at high latitudes the OBP variability dominates the sea level variability at seasonal-to-decadal time scales. The diagnostic OBP based on barotropic vorticity equation has a good correlation with the observations, indicating that wind forcing plays an important role in the variability of the OBP in the Southern Ocean. The unique interannual patterns of OBP in the Southern Ocean are closely associated with El Niño-Southern Oscillation (ENSO) and Southern Annular Mode (SAM). Regression analysis indicates that ENSO and SAM influence the OBP through altering the Ekman transport driven by surface wind. The leading pattern of OBP from PCOM are very similar to observations. Sensitive experiments of PCOM show that surface wind forcing explains the observed OBP variability quite well, confirming the importance of wind forcing and related oceanic processes. In the eastern South Pacific, the averaged OBP shows a decrease (increase) trend before (after) 2011, reflecting the reverse trend in westerly wind. In the South Indo-Atlantic Ocean, the averaged OBP has a weak increase trend during 2003–2016.

Key words: ocean bottom pressure, Southern Ocean, interannual variability, PCOM

Citation: Xiong Xiaoqin, Cheng Xuhua, Ou Niansen, Feng Tao, Qin Jianhuang, Chen Xiao, Huang Rui Xin. 2022. Dynamics of seasonal and interannual variability of the ocean bottom pressure in the Southern Ocean. Acta Oceanologica Sinica, 41(5): 78–89, doi: 10.1007/s13131-021-1878-z

1 Introduction

Ocean bottom pressure (OBP) summarizes the total effect of the atmosphere and ocean mass above the seafloor. In general, the OBP variability is driven by three processes, i.e., redistribution of oceanic mass forced by local winds and ocean circulations (Gill and Niller, 1973; Stepanov and Hughes, 2006; Cheng et al., 2013), water mass flux (Chambers et al., 2017) and sea level pressure (Ponte, 1999). Change in OBP can translate into equivalent change of sea level by $p_b/\rho g$, and p_b is the change of OBP, ρ is the density of sea water, g is the gravitational acceleration. Globally, OBP change accounts for approximately 60% of the global mean sea level rise (Chambers et al., 2017). Therefore, new insights into OBP variability can advance our understanding of the ocean heat storage, sea level, the vertical structure of oceanic variability, and other aspects of ocean circulation and climate.

The Southern Ocean is an important part of the global overturning circulation, global climate system, deep water morphology, and carbon cycle (Meredith et al., 2011). The changes of OBP in the Southern Ocean are closely related to the variations of zonal circumpolar circulation through geostrophic adjustment toward equilibrium (Meredith et al., 2011). Given its close relationship with the zonal transport variations and meridional overturning circulation, it is important to understand what controls the OBP variations in the Southern Ocean.

Before the launching of Gravity Recovery and Climate Experiment (GRACE), studies of OBP mainly relied on sparse observations, theoretical diagnosis and numerical models (e.g., Gill and Niller, 1973; Ponte, 1999; Vivier et al., 2005; Cabanes et al., 2006). Ponte (1999) firstly simulated global OBP using a volume conserved model. The model results illustrated high amplitude of OBP in the Southern Ocean. Using sea level data and a barotropic model, Vivier et al. (2005) found the barotropic component dominates the sea level variations at high latitudes in the Southern Ocean. The variations in the sea level and OBP at various time scales in the South Atlantic have been explained by basin-wide Sverdrup transport which is driven by local wind stress, Ekman pumping, and barotropic/baroclinic Rossby waves (Cabanes et al., 2006).

Since 2002, the launching of GRACE has made it possible to monitor global and regional OBP variability, and reveal OBP's responses to the global and regional changes in the climate system. From sub-seasonal to interannual time scales, OBP changes are

Foundation item: The National Key R&D Program of China under contract No. 2018YFA0605703; the National Natural Science Foundation of China under contract Nos 41876002 and 41876224.
*Corresponding author, E-mail: xuhuacheng@hhu.edu.cn

consistent with sea level changes at high latitudes in the Southern Ocean (Quinn and Ponte, 2012; Piecuch et al., 2013). The most significant seasonal OBP changes occur in continental and coastal regions at high latitudes. In the Southern Ocean, the amplitude of seasonal OBP signals is on the order of 4 cm to 5 cm (Peralta-Ferriz et al., 2017). The interannual OBP variability is remarkably large in the South Pacific and the South Indian Oceans (Piecuch et al., 2013; Ponte and Piecuch, 2014), which accounts for a large part of local total sea level variability. A number of studies have reported the correlations between OBP and Southern Annular Mode (SAM) in the South Hemisphere (e.g., Zlotnicki et al., 2007; Bergmann and Dobslaw, 2012; Ponte and Piecuch, 2014; Makowski et al., 2015; Liau and Chao, 2017). El Niño-Southern Oscillation (ENSO) also has a noticeable impact on global and regional OBP variations (Song and Zlotnicki, 2008; Boening et al., 2012; Cazenave et al., 2012, 2014; Fasullo et al., 2013; Wang et al., 2015). However, only a few studies have investigated the impact of ENSO on OBP variations in the Southern Ocean. OBP in the Southern Ocean also exhibits significant decadal trends during the GRACE era, which were associated with the change of surface winds in the southern hemisphere (Johnson and Chambers, 2013; Makowski et al., 2015; Peralta-Ferriz et al., 2017).

Over the past several decades, numerical oceanic models have experienced pronounced improvements. These models have been used to study the OBP variations in the world oceans that were difficult to observe by the traditional instruments (e.g., Stammer et al., 1996; Ponte, 1999; Huang et al., 2001; Stepanov and Hughes, 2006; Brunnabend et al., 2011; Androsov et al., 2020). Most ocean models were based on the volume conservation associated with the Boussinesq approximations. In these models, a globally uniform, time-dependent factor calculated from the volume-averaged density change is used to compensate for the Boussinesq approximation (Greatbatch, 1994). Previous studies indicated that the Boussinesq models can predict sea level changes with acceptable accuracy (Greatbatch, 1994; Dukowicz, 1997). However, they replace mass conservation with volume conservation, and thus violate conservation law of mass and energy. Any diabatic process will cause faulty mass sources or sinks, and produce a faulty pressure gradient force (Huang et al., 2001). To overcome the limitation of the Boussinesq approximations, mass conservation oceanic models are needed, which can accurately handle the conservation of heat content, salt content and total mass in the ocean; thus, such models can more accurately predict ocean bottom pressure, sea level change and study the effect and response of the ocean during the course of climate changes.

Overall, features and dynamics of OBP variations in the Southern Ocean remain an interesting issue, and have not been fully investigated. To date, the accumulating GRACE record is more than one and half decades long; such data provides an unprecedented view of OBP variability on the global and regional scales. Combined with numerical models based on mass conservation, the dynamics of OBP in the Southern Ocean can be examined more systematically. In this study we use both observational data and results from a mass-conservation model to explore the multiscale characteristics of the OBP in the Southern Ocean; in particularly, we will explore the impacts of wind and other atmospheric factors on the OBP variability.

The remainder of this paper is organized as follows. Model configurations and methods used in this study are introduced in Section 2. In Section 3, the seasonal and interannual variabilities as well as the dynamics are discussed. Finally, Section 4 presents the conclusions.

2 Data and methods

2.1 *Data*

Monthly OBP data used in this study are GRACE data of Release Level 6 (RL06) from the Center for Space Research (CSR) of the University of Texas. The data has a resolution of 1°×1° and spans from 2003 to 2016. Linear interpolation was performed to reconstruct the values in months to avoid missing values. The monthly sea level anomaly (SLA) data with a resolution of 0.25°×0.25° for 2003–2016 are obtained from the multi-satellite convergence sea level anomaly data released by the European Copernicus Marine Environment Monitoring Service (CMEMS). Temperature and salinity data for 2004–2016 with vertical 58 layers and a spatial resolution of 1°×1° are from the monthly mean global ocean Argo grid dataset (BOA-Argo; Li et al., 2017), which can be downloaded on http://www.argo.org.cn/.

Atmospheric variables, such as monthly wind data for 2003–2016 are obtained from two reanalysis products: the National Centers for Environmental Prediction-National Center for Atmospheric Research (NCEP-NCAR; Kalnay et al., 1996) with a horizontal resolution of 2.5° and the European Centre for Medium-Range Weather Forecasts (ECMWF) Re-Analysis-Interim (ERA-Interim) Reanalysis data with a horizontal resolution of 0.25°. The Ekman transport derived from different reanalysis products share similar features (figures not included). Therefore, only results from ERA-Interim are shown. Monthly wind stress and sea level pressure (SLP) data over 2003–2016 are used as forcing condition for model runs. Heat flux and freshwater flux are obtained from Objectively Analyzed Air-sea Fluxes (OAFlux) of Woods Hole Oceanographic Institute (http://oaflux.whoi.edu). In this study, the Niño 3.4 index is used as the ENSO index, which is downloaded from https://www.esrl.noaa.gov/psd/gcos_wgsp/Timeseries/Nino34/. The SAM index is defined as the difference of the normalized monthly zonal mean SLP between 40°S and 65°S (Marshall, 2003), which is available from https://legacy.bas.ac.uk/met/gjma/sam.html.

The statistical significance of the correlation coefficient is tested with the Student *t*-test, which determines whether two populations express a significant difference among the population means.

2.2 *Methods*

According to Thomson and Tabata (1989), the steric sea level variability (ΔZ) contains two terms: the thermosteric sea level variability (ΔZ_T) and the halosteric sea level variability (ΔZ_S), that is

$$\begin{aligned}\Delta Z &= \Delta Z_T + \Delta Z_S = \int_{Z_1}^{Z_2} \alpha \Delta T \mathrm{d}z - \int_{Z_1}^{Z_2} \beta \Delta S \mathrm{d}z \\ &= -\int_{Z_1}^{Z_2} \frac{1}{\rho}\frac{\partial \rho}{\partial T}\Delta T \mathrm{d}z - \int_{Z_1}^{Z_2} \frac{1}{\rho}\frac{\partial \rho}{\partial S}\Delta S \mathrm{d}z,\end{aligned} \tag{1}$$

where a and β are the thermal expansion coefficient and salt compression coefficient of seawater, respectively; ρ is the seawater density (unit: kg/m^3); T is the seawater temperature (unit: °C); S is the seawater salinity (unit: psu); Z is the depth (unit: m). According to Argo data, Z_1 and Z_2 here are set as 0 m and 2 000 m, respectively.

The barotropic vorticity equation is used to quantify the dominant atmospheric forcing mechanism and the oceanic response

process to OBP variability (Boening et al., 2011):

$$\frac{\partial}{\partial t}\nabla^2\eta - \frac{f^2}{gH}\frac{\partial \eta}{\partial t} + \beta\frac{\partial \eta}{\partial x} - \frac{f}{H}\left(\frac{\partial \eta}{\partial x}\frac{\partial H}{\partial y} - \frac{\partial \eta}{\partial y}\frac{\partial H}{\partial x}\right) + \nabla\cdot\left(\frac{r}{H}\nabla\eta\right) = \frac{f}{\rho g}\nabla\times\frac{\tau}{H} - \frac{f^2}{g^2H\rho}\frac{\partial P_a}{\partial t}, \quad (2)$$

where η is the barotropic sea surface height (equivalent to OBP; unit: m); f is the Coriolis parameter; ϕ is latitude; β is the change of Coriolis parameter with latitude, that is $\beta = \mathrm{d}f/R\mathrm{d}\phi$, R is the radius of the earth; τ is wind stress (unit: N/m^2); P_a is the sea surface pressure (unit: Pa); $-H$ is the depth of the seafloor (unit: m); r is the bottom friction coefficient; g is the gravitational acceleration (9.8 m/s^2). The first and second terms on the left-hand side represent the rate of relative vorticity convergence and vorticity change caused by water column stretching; the third term represents the planetary vorticity gradient; the fourth and fifth terms are the topographic stretching term and the dissipation term; the first and second terms on the right side represent the effects of wind stress curl and sea surface pressure.

Previous study indicated that the wind forcing and topographic effect are important (Boening et al., 2011). Furthermore, time dependent terms can be omitted. Hence, Eq. (2) can be reduced to the following approximation:

$$\beta\frac{\partial \eta}{\partial x} \approx \frac{f}{\rho g}\nabla\times\frac{\tau}{H} - \frac{f}{H}\left(\frac{\partial \eta}{\partial x}\frac{\partial H}{\partial y} - \frac{\partial \eta}{\partial y}\frac{\partial H}{\partial x}\right). \quad (3)$$

Integrating Eq. (3) leads to a relation between the zonal variability of OBP and the zonal accumulated effect of wind stress curl:

$$\eta^x \sim \int_{xe}^{x}\frac{1}{\beta}\left[\frac{f}{\rho g}\nabla\times\frac{\tau}{H} - \frac{f}{H}\left(\frac{\partial \eta}{\partial x}\frac{\partial H}{\partial y} - \frac{\partial \eta}{\partial y}\frac{\partial H}{\partial x}\right)\right]\mathrm{d}x + \eta^{xe}, \quad (4)$$

where the term η^{xe} is OBP at the starting station, which can be obtained from GRACE data. This equation can be used to explore the relation between the variability of OBP and wind stress curl and topographic effect.

2.3 *Model*

In this study, an Ocean General Circulation Model (OGCM) based on mass conservation, Pressure Coordinate Ocean Model (PCOM), is used. PCOM was originally developed by Huang et al. (2001) and further improved by Zhang et al. (2014). As a model based on mass conservation, PCOM can provide more accurate simulations of sea surface height and OBP than the models based on volume conservation, in particular for the cases involving diabatic processes associated with climate changes.

Ou et al. (2016) recently showed that the simulation performance of the PCOM 1.0 in current, salinity and temperature fields are comparable to those of the Coordinated Ocean-ice Reference Experiments (COREs) model. The PCOM model has 60 pressure layers with a horizontal resolution of 1°×1°. Instead of a vertical mixing scheme, PCOM adopts the climatological value of turbulent mixing coefficients calculated by Zhang et al. (2014) (see Huang et al. (2001) and Zhang et al. (2014) for more details of PCOM). A spin-up run was performed for 600 years from a static state and forced by the climatological monthly mean atmospheric forcing, including fresh water flux, surface heat flux, surface wind and SLP. By including SLP as an upper boundary condition, the PCOM can simulate the OBP variability more accurately. The initial temperature and salinity for the spin-up run are derived from World Ocean Atlas 2009 (Antonov et al., 2010; Locarnini et al., 2010). Restarting from the spin-up run, three experiments have been carried out for 29 years. In this study, model outputs over 2003–2016 are used. The control run (Exp. 1) is forced by daily atmospheric forcing during 1990–2018. Exp. 2 and Exp. 3 are the same as the control run, except excluding SLP forcing and wind forcing, respectively.

3 Seasonal and interannual variability of OBP in the Southern Ocean

3.1 *Seasonal variability*

SLA consists of contributions from OBP and steric sea level. Figure 1 shows the seasonal variability of SLA, steric sea level and OBP in the Southern Ocean for the period of 2003–2016. At mid latitudes (30°S to 55°S), the pattern of steric sea level seasonal variability is quite similar to that of SLA (Figs 1a and b), whereas the pattern of OBP is different (Fig. 1c).

The relations between steric sea level, sea level and OBP can be seen clearly from the ratio of these terms. As shown in Fig. 2a, at middle latitudes, the ratio of steric sea level to sea level is positive, while the ratio of OBP to sea level is negative or weakly positive, indicating that steric contribution is the dominating term for sea level at mid latitudes. At high latitudes (south of 55°S), positive values of SLA (Fig. 1a) occur during austral summer (DJF) and reach maximum (above 4 cm); however, SLA becomes negative and reaches the minimum (below 4 cm) during austral winter (JJA). The ratio of OBP to sea level is about 1, indicating the dominating role of OBP to sea level variability on seasonal time scales (Figs 1c and 2b).

Vectors in Fig. 1c represent the Ekman transport. It is clear that the positive (negative) anomaly of OBP in the South Indian Ocean and South Atlantic Ocean (south of 60°S) during austral summer (winter) is attributed to the convergence (divergence) of the Ekman transport anomalies. Thus, Ekman transport induced by wind stress dominates the seasonal variability of OBP in the Southern Ocean, especially at high latitudes. Our analysis is consistent with Peralta-Ferriz et al. (2017). They concluded that the most significant seasonal OBP changes occur in ocean and coastal regions at high latitudes, usually reaching 4 cm to 5 cm equivalent root mean square (RMS) sea level.

Seasonal variability of OBP from PCOM simulation is shown in Fig. 3a, which shows similar patterns to observations. In fact, PCOM simulations can capture the positive and negative anomalies at the high latitudes of Southern Indian Ocean and Atlantic Ocean during austral summer and winter very well. We also explored the roles of SLP and wind on OBP simulation in the Southern Ocean (Figs 3b and c). Comparing Figs 3a and b, there is almost no difference in their spatial distribution, indicating that on seasonal time scales the SLP has little contribution to the change of OBP due to the static adjustment of SLP. It can also be seen in Fig. 3c that the impact of SLP on seasonal variability of OBP is almost negligible, except for the east coast of South America. The sensitive experiments of PCOM further suggest that the seasonal variability of OBP in the Southern Ocean is mainly generated by wind forcing.

3.2 *Interannual variability of basin mean observed and diagnostic OBP*

As discussed in Section 3.1, the seasonal variability of OBP in the South Indian Ocean and South Atlantic Ocean are quite strong and rather similar. Therefore, we select two special regions in the Southern Ocean: the eastern South Pacific Ocean (150°–80°W) and the South Indo-Atlantic Ocean (60°W–10°E).

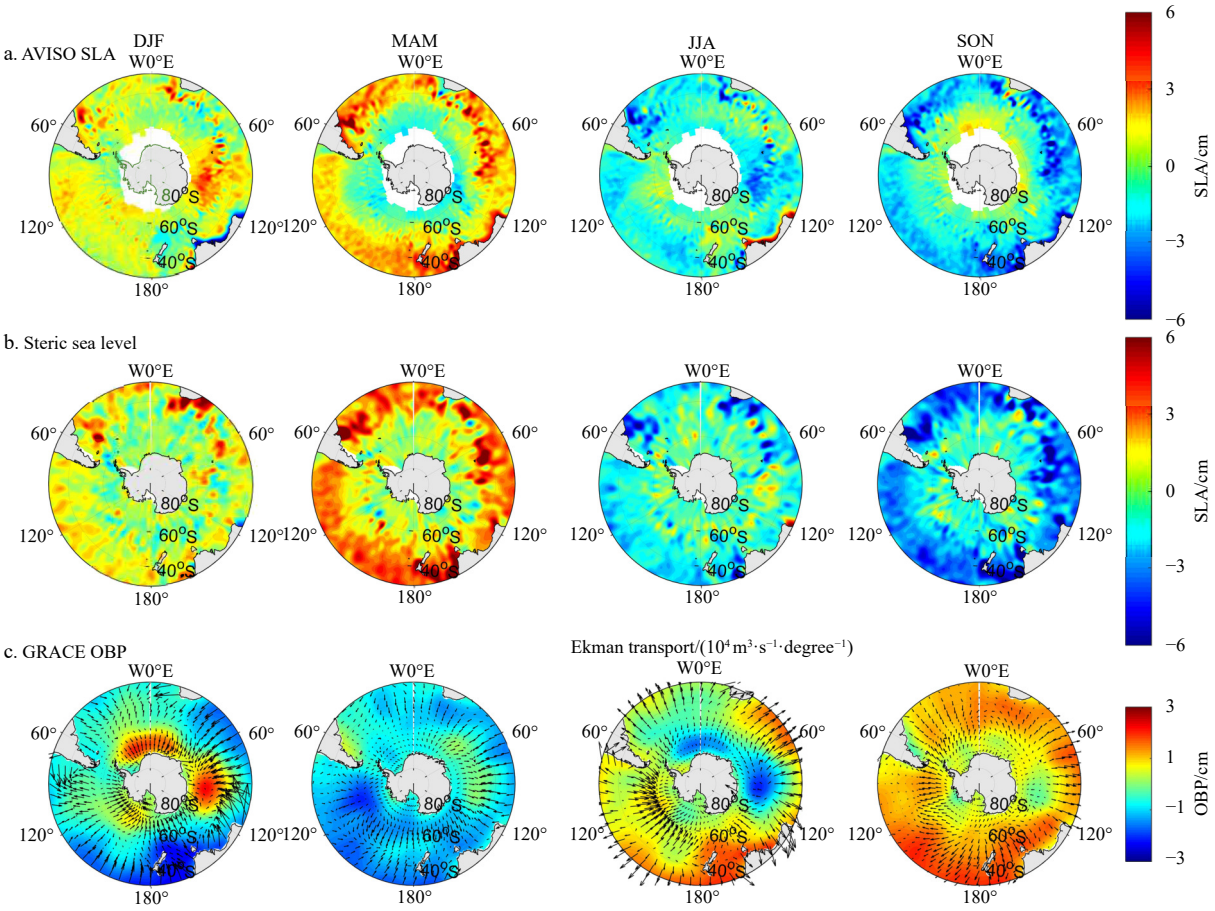

Fig. 1. Seasonal variability of AVISO SLA (top, a), steric sea level (middle, b), and GARCE OBP (bottom, c) in the Southern Ocean for the period of 2004–2016 (color shading, in unit of cm). From left to right, each column represents austral summer (DJF, December, January and February), autumn (MAM, March, April and May), winter (JJA, June, July and August), and spring (SON, September, October and November), respectively. The vectors in c represent Ekman transport anomaly (in unit of 10^4 $m^3/(s\cdot(^o))$ calculated from ERA-interim. Climatological annual mean has been removed.

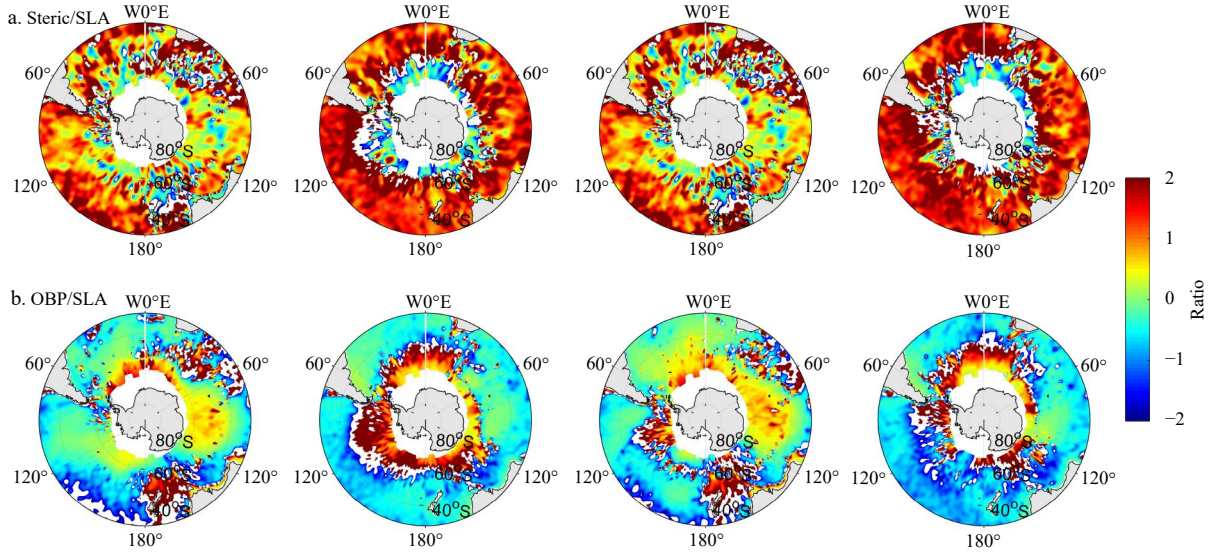

Fig. 2. Ratio of steric sea level to sea level anomaly (a), and ratio of ocean bottom pressure to sea level anomaly (b).

The interannual variability of SLA, steric sea level and OBP time series averaged in these two regions are shown in Fig. 4. The correlation coefficients between SLA and OBP in these two regions are 0.87 and 0.86 (significant at 99% confidence level), which are much higher than that between SLA and steric sea level (The correlation 0.26 and 0.31, respectively). Hence, the interannual vari-

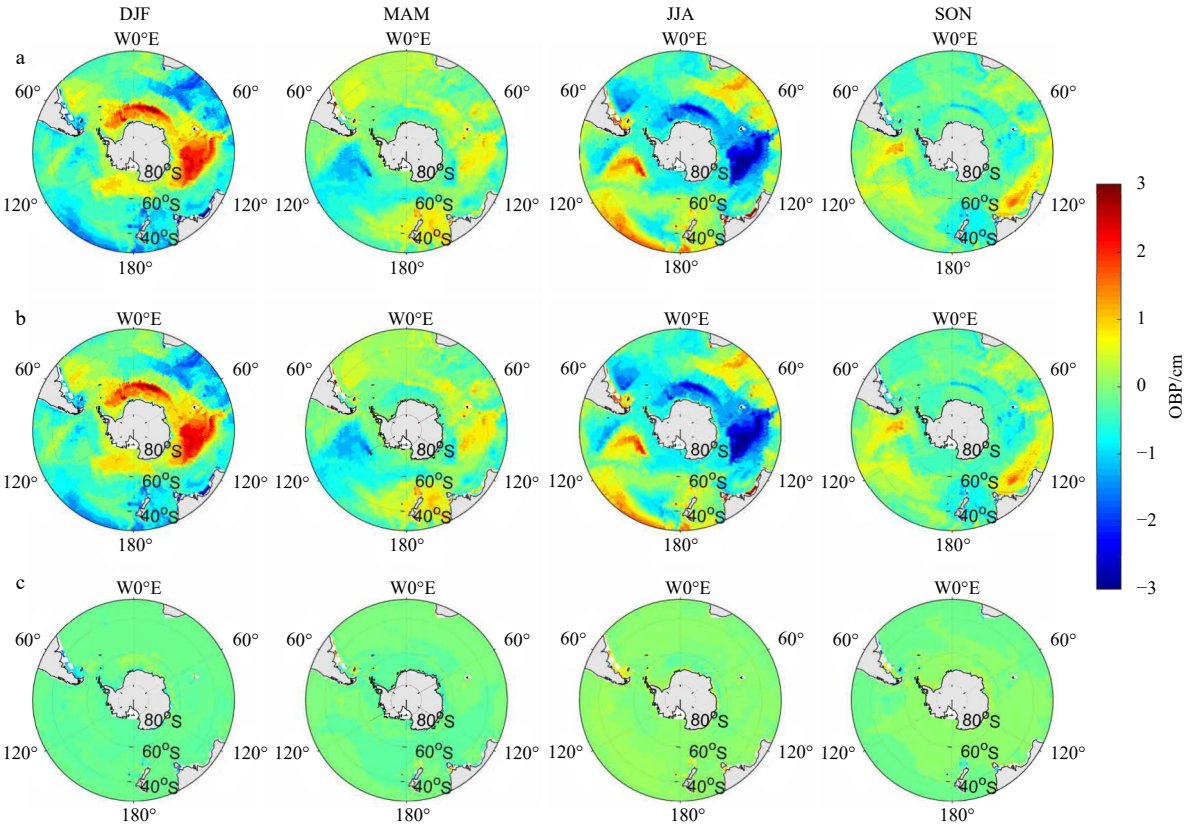

Fig. 3. Seasonal variability of OBP (in unit of cm) obtained from PCOM runs: a. in control run (Exp. 1), b. without air pressure forcing (Exp. 2), c. without wind forcing (Exp. 3) averaged in austral summer (DJF, December, January and February; first column), autumn (MAM, March, April and May; second column), winter (JJA, June, July and August; third column), and spring (SON, September, October and November; fourth column) in the Southern Ocean from 2004 to 2016. Climatological annual mean has been removed.

ability of SLA is closely linked to the interannual variability of OBP in the Southern Ocean. Previous studies have also shown that at high latitudes, OBP variability resembles the sea level variations at seasonal and interannual time scales (Vivier et al., 2005; Quinn and Ponte, 2012; Piecuch et al., 2013). Moreover, OBP shows a weak decreasing trend before 2010 and an increasing trend after 2010 in the eastern South Pacific Ocean, and an obvious increasing trend in the South Indo-Atlantic Ocean for the period of 2004–2016. These interesting results will be discussed in Section 4.

To better understand the relationship between wind stress and OBP variability, barotropic vorticity equation (Eq. (4)) is used to quantify the contribution of wind forcing and topographic effect to the interannual variability of OBP following Boening et al. (2011). Figure 5 shows the reconstructed OBP indices in the Southern Ocean. Due to land mass distribution, reconstructions of OBP are carried out in three basins. The reconstructed OBP indices by wind stress have high correlation coefficients (over 0.77, significant at 99% confidence level) with OBP indices calculated by GRACE. The correlations between them are still significant after their trends are removed (figure not shown). It is evident that the interannual variability of OBP is dominated by the barotropic response to wind stress in the Southern Ocean. The topographic effect has a relatively strong amplitude due to steep bottom topography, which play a secondly role in OBP variations.

3.3 *Spatio-temporal variability of OBP*

The empirical orthogonal function (EOF) analysis is applied to further explore the spatial structure and temporal variations of OBP in the South Pacific Ocean and South Indo-Atlantic Ocean. The regression between Ekman transport and EOF's principal components (PCs) are also made. The trends of GRACE OBP and Ekman transport have been removed before performing EOF analysis. The first and second EOF modes with their PCs calculated by GRACE OBP for the period of 2003–2016 in the South Pacific Ocean are shown in Fig. 6. The EOF1 and EOF2 explain 52% and 12% of the total variance, respectively. The EOF1 is characterized by the positive OBP anomalies at the high latitudes of the South Pacific Ocean, and the center of maximum value is around 50°–65°S, 150°–90°W (Fig. 6a). The distribution of Ekman transport is consistent with EOF1, displaying convergence (divergence) over positive (negative) OBP. The EOF2 is depicted as a dipole in southeast-northwest direction with opposing centers of action (Fig. 6b), where the convergence (divergence) Ekman transport is accompanied by positive (negative) OBP anomalies. The correlation coefficient between PC1 and Niño 3.4 index is 0.49 (Fig. 6e, significant at 90% confidence level), and the correlation coefficient between PC2 and SAM index is 0.61 (Fig. 6f), which is significant at 99% confidence level.

PCOM is also capable of capturing the interannual variability of OBP quite well. Comparing Figs 6a and b with Figs 6c and d, the characteristics of the leading two EOF modes of observed OBP are well reproduced in the PCOM control run (Exp. 1). In the South Pacific Ocean, positive center and a dipole can also be clearly seen in EOF1 and EOF2 of PCOM OBP, respectively (Figs 6c and d). The vectors are the regression of Ekman transport against the time series of the first two EOF components of PCOM simulated OBP. The EOF1 and EOF2 explain 37% and 13% of the

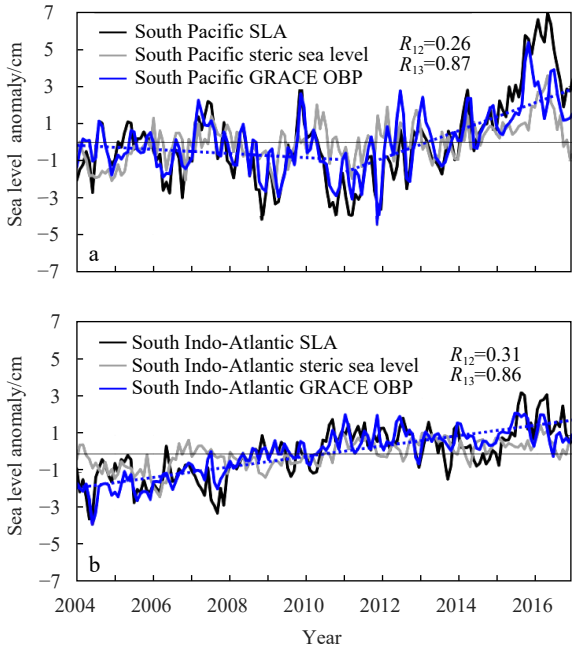

Fig. 4. Time series of GRACE OBP anomaly (solid blue lines), SLA (solid black line), steric sea level anomaly (solid gray line) averaged in the South Pacific (40°–60°S, 150°–90°W) (a) and in the South Indo-Atlantic Ocean (40°–60°S, 60°W–120°E) (b) from 2004 to 2016. The anomalies are calculated by subtracting climatological annual cycle. The linear trends of GRACE OBP are displayed as blue dashed lines. In a, R_{12} is the correlation coefficient between South Pacific SLA and South Pacific steric sea level, and R_{13} is the correlation coefficient between South Pacific SLA and South Pacific steric GRACE OBP. In b, R_{12} is the correlation coefficient between South Indo-Atlantic SLA and South Indo-Atlantic steric sea level, and R_{13} is the correlation coefficient between South Indo-Atlantic SLA and South Indo-Atlantic steric GRACE OBP.

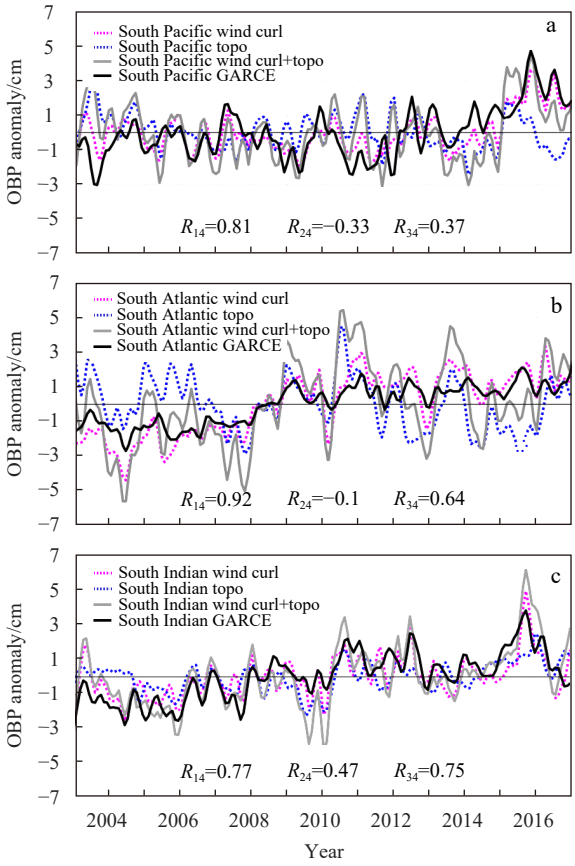

Fig. 5. Time series of GRACE OBP anomaly (black lines), OBP anomaly reconstructed from wind forcing (pink lines) and topographic (topo) effect (blue lines) and sum of two terms (gray lines) averaged in the eastern South Pacific (40°–60°S, 150°–80°W) (a), the South Atlantic (40°–60°S, 60°–0°W) (b) , and the South Indian Ocean (40°–60°S, 30°–120°E) (c) from 2003 to 2016. The blue dashed lines are the trend of the GRACE OBP time series. The unit of the *y*-axis is cm. The anomalies are calculated by subtracting climatological annual cycle. In a, R_{14} is the correlation coefficient between South Pacific wind curl and South Pacific GRACE, R_{24} is the correlation coefficient between South Pacific topo and South Pacific GRACE, and R_{34} is the correlation coefficient between South Pacific wind curl+topo and South Pacific GRACE. In b, R_{14} is the correlation coefficient between South Atlantic wind curl and South Atlantic GRACE, R_{24} is the correlation coefficient between South Atlantic topo and South Atlantic GRACE, and R_{34} is the correlation coefficient between South Atlantic wind curl+topo and South Atlantic GRACE. In c, R_{14} is the correlation coefficient between South Indian wind curl and South Indian GRACE, R_{24} is the correlation coefficient between South Indian topo and South Indian GRACE, and R_{34} is the correlation coefficient between South Indian wind curl+topo and South Indian GRACE.

total variance, respectively. The correlation coefficient of PC1 between GRACE OBP and PCOM OBP is 0.78 (significant at 99% confidence level), but the correlation coefficient of PC2 of them is 0.28 (Figs 6e and f). The PC1 of simulated OBP also has a close relationship with the Niño 3.4 index (r=0.55, significant at 95% confidence level), while PC2 has no statistical connection with SAM index (r=–0.02).

The EOF analysis of GRACE OBP in the South Indo-Atlantic Ocean is shown in Fig. 7, and the vectors are also the regression between Ekman transport and PCs. The EOF1 and EOF2 explain 34% and 14% of total variance, respectively. The EOF1 is featured by positive OBP anomalies around 40°–60°S, 30°–120°E in the South Indian Ocean, accompanied with the Ekman transport convergence around 50°S (Fig. 7a). The EOF2 shows a center of negative anomalies of OBP in the South Indo-Atlantic Ocean around 50°–60°S, 60°W–30°E (Fig. 7b). The negative anomaly centers are closely linked to the divergence of Ekman pumping anomaly. The correlation coefficients between the two PCs and SAM index are 0.54 and 0.43, respectively (Figs 7e) (both significant at 99% confidence level). The SAM index used in this study is defined as the difference of the normalized monthly zonal mean SLP between 40°S and 65°S (Marshall, 2003); thus, it is not surprising for the good relationship between both PCs. On the other hand, PCs calculated by GRACE OBP in the South Indo-Atlantic Ocean do not have significant relation with Niño 3.4 index.

EOF1 and EOF2 of PCOM OBP in the South Indo-Atlantic Ocean are also shown in Figs 7c and d, which explain 31% and 17% of total variance, respectively. Although the centers in EOFs for PCOM OBP are weaker than that for GRACE, the spatial structures are clearly reproduced in the PCOM simulation, i.e., positive center (40°–60°S, 60°–120°E) in EOF1 corresponds to Ekman transport convergence and negative center (50°–65°S, 10°–55°E)

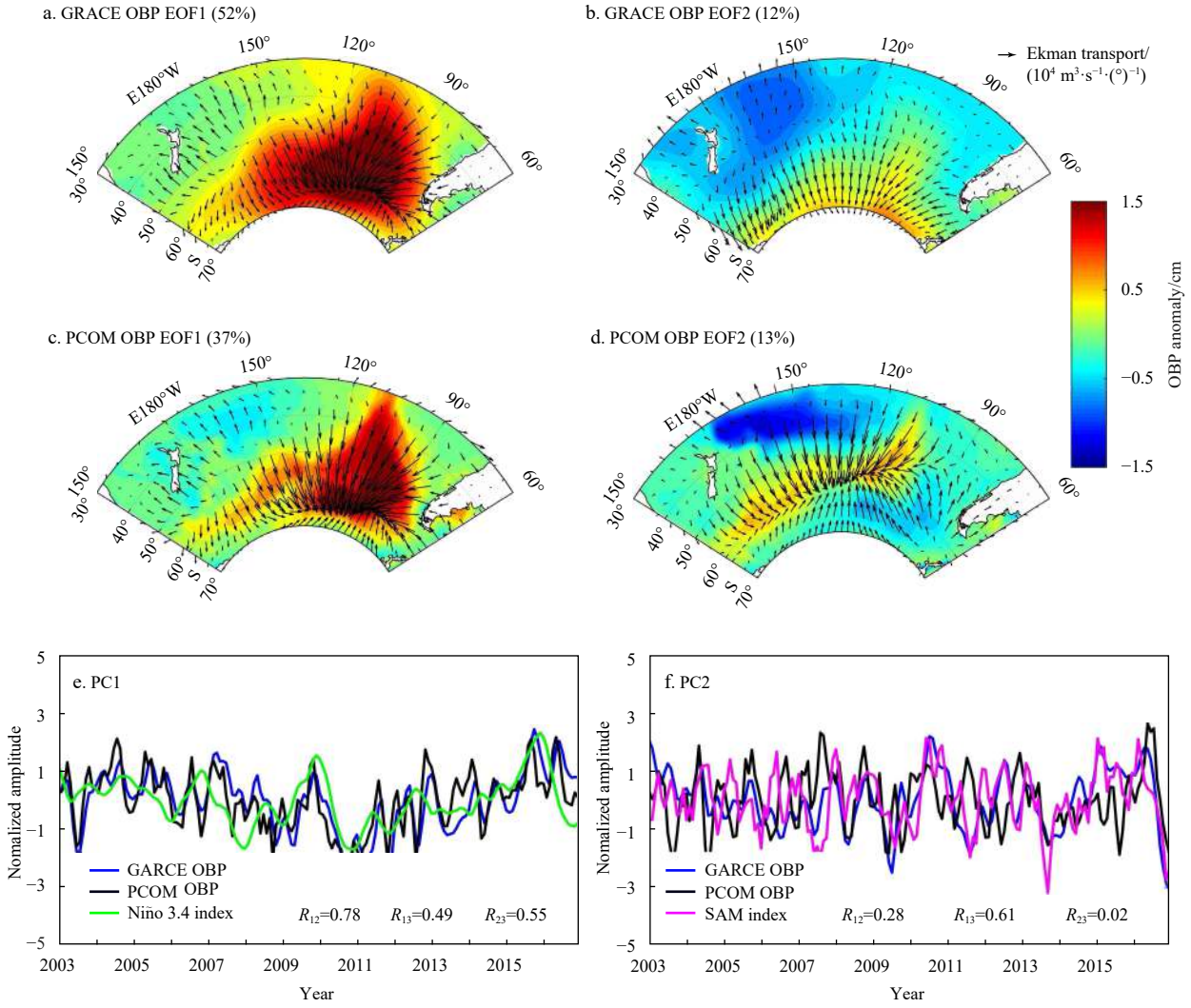

Fig. 6. The spatial structures of the first EOF mode (a) and the second EOF mode (b) of the GRACE OBP (shade; cm) in the South Pacific Ocean from 2003 to 2016, and the spatial structures of the first EOF mode (c) and the second EOF mode (d) of the PCOM OBP (shade; cm) in the South Pacific Ocean from 2003 to 2016, and the rincipal component (PC) time series of the first EOF mode (e) and the second EOF mode (f). The green line in f represents the Niño 3.4 index. The pink line in f represents the SAM index. The vectors denote Ekman transport (10^4 m^3/(°)) regressed on to each time series. Monthly climatology has been removed before EOF analysis.

in EOF2 is accompanied by Ekman transport divergence. The correlation coefficient between PC1 and SAM index is 0.69, which is significant at 99% confidence level. The first two EOF mode time series between the GRACE observed and PCOM simulated OBPs are well correlated, with the correlation coefficients of 0.78 and 0.71, respectively (both are significant at 99% confidence level). Figure 7 indicates that the PCOM reproduced the interannual variability quite well in the South Indo-Atlantic Ocean.

The high correlation between PCs and Niño 3.4 index (or SAM index) (Figs 6 and 7) inspired us to examine OBP variability associated with ENSO and SAM. As shown in Fig. 8a, regression map of GRACE OBP shows positive value (1 or even higher) coincident with Ekman convergence at high latitudes (around 50° –70°S) in the South Pacific Ocean. Such a pattern is quite similar to that of EOF1 in the South Pacific Ocean (Fig. 6a). The regression map of GRACE OBP and Ekman transport with SAM index is shown in Fig. 8b. The positive center of OBP companied by Ekman transport convergence occurs around 40°–60°S in the South Indian Ocean, which has a close relation with EOF1 in the South Indo-Atlantic Ocean (Fig. 7a). Moreover, a dipole pattern of OBP in the southeast-northwest direction appears in the regression map in the South Pacific Ocean (resembling EOF2, Fig. 6b). Figure 8c shows the regression maps of PCOM OBP and Ekman transport with Niño 3.4 index. It is noted that the positive value of the regression coefficient of PCOM OBP is obvious in Southern Pacific Ocean, companies with the Ekman transport convergence. Such a pattern is similar to the regression map of GRACE OBP (Fig. 8a) and EOF1 in the South Pacific Ocean (Figs 6a and c). The distribution of regression of PCOM OBP and Ekman transport with SAM index is shown in Fig. 8d, and it is very similar to that of GRACE OBP (Fig. 8b).

The regression maps of SST and SLP with PCs (Fig. 9) further prove the close relationship of OBP variability with ENSO and SAM. The regression map of SST shows an “ENSO-like” pattern with PC1 for both GRACE OBP and PCOM OBP (Figs 9a and d). The distribution pattern (Figs 8b and d) of the regression maps are closer to circular annular mode distribution and the meridional see-saw SLP anomalies are obtained with PCs in GARCE

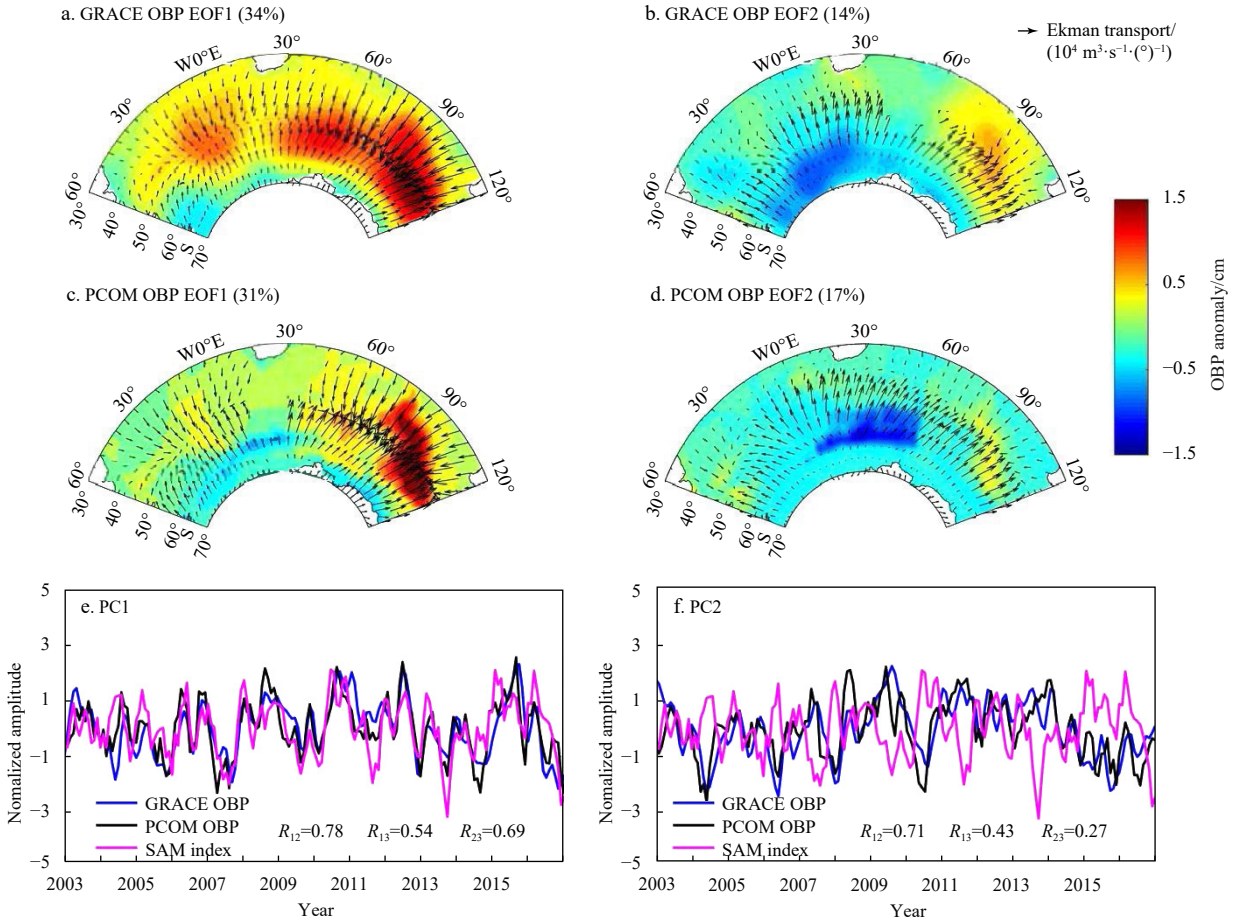

Fig. 7. The structures of the first EOF mode (a) and the second EOF mode (b) of the GRACE OBP (shade; cm) and the spatial structures of the first EOF mode (c) and the second EOF mode (d) of the PCOM OBP (shade) in the South Indo-Atlantic Ocean from 2003 to 2016, and the principal component (PC) time series of the first EOF mode (e) and the second EOF mode (f). The pink lines in e and f represent the SAM index. The vectors denote Ekman transport ($m^3/(°)$) regressed on to each time series. Monthly climatology has been removed before EOF analysis.

(Figs 9b and c) and PCOM (Figs 9e and f), which demonstrates the impact of SAM on OBP via altering wind field. The slight difference between simulation and observations indicates that changes in the observed OBP have other impact factors, but the contribution of the wind field is dominant. Thus, it is concluded that ENSO and SAM play important roles in interannual OBP variability in the Southern Ocean, by modulating the Ekman transport driven by sea surface winds. The strong interannual variability of OBP is located at high latitudes in the Southern Ocean (Fig. 10a). The high variance centers correspond well to patterns of OBP EOFs (Figs 6a and 7a). PCOM control run reproduces the high variance centers quite well (Fig. 10b). The pattern and amplitude in Exp. 2 are almost the same as that in control run (Figs 10b and c), indicating that SLP forcing is not important in interannual variability of OBP. The variance of OBP in Exp. 3 is extremely weak (Fig. 10d), which further confirms that the wind forcing dominates the interannual variability of OBP in the Southern Ocean.

As shown in Figs 4 and 5, remarkable trends are captured in GRACE OBP indices and reconstructed OBP indices. The OBP indices show an increasing trend in the South Pacific Ocean after 2010, and in the South Indo-Atlantic Ocean from 2003 to 2016. Such trends account for the increasing trends of SLA during these periods. GRACE OBP in the South Pacific Ocean shows a weakly decreasing trend before 2010 (Fig. 11a) and an obvious increasing trend (over 1 cm/a) after 2010 (Fig. 11b). The correlation coefficient is 0.55 (significant at 99% confidence level) between Niño3.4 indices and PC1 calculated by GRACE OBP in the South Pacific Ocean (Fig. 6e). Furthermore, EOF1 is dominated by natural variability. In particular, the Interdecadal Pacific Oscillation (IPO) (Henley et al., 2015), whose phase was reversed from positive (El Niño-like state) to negative in the late 2010s. The Ekman transports over the South Pacific Ocean are enhanced during this decade of warming. In the South Indo-Atlantic Ocean (Fig. 11c), the OBP has an increasing trend, which was possibly due to fresh water input associated with the glaciers melting. The contribution of wind forcing was not significant, since the trend of Ekman transport was weak (Fig. 11f).

Figures 11d–f show the trend of Southern Ocean OBP simulated by PCOM. The OBP trend in the Ocean is well simulated in PCOM (Figs 11d and e). In comparison, the PCOM simulation in the South Indo-Atlantic Ocean is not so good (Fig. 11f), and the difference is likely due to the fact that fresh water input associated with the glaciers melting is not included in the current version of PCOM model.

4 Conclusions

In this study, we investigated the seasonal and interannual variabilities of OBP in the Southern Ocean and the possible im-

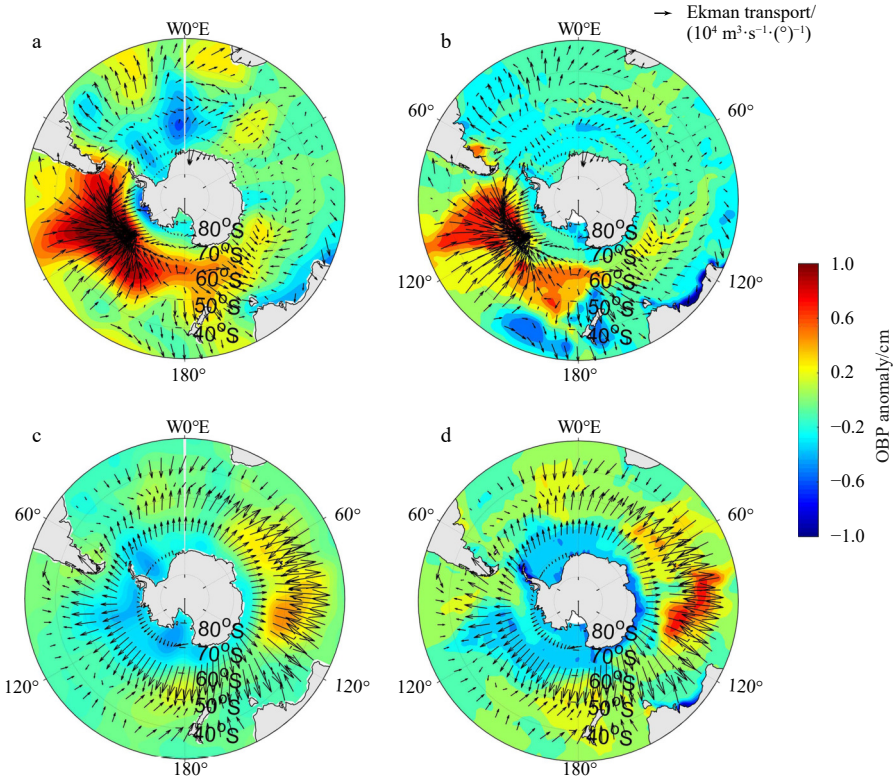

Fig. 8. GRACE OBP anomaly (shading) and Ekman transport anomaly (vectors) regressed onto Niño 3.4 index (a) and SAM index (b) and PCOM OBP anomaly (shading) Ekman transport anomaly (vectors) regressed onto Niño 3.4 index (c) and SAM index (d) from 2003 to 2016. Ekman transport anomaly data are from ERA-Interim.

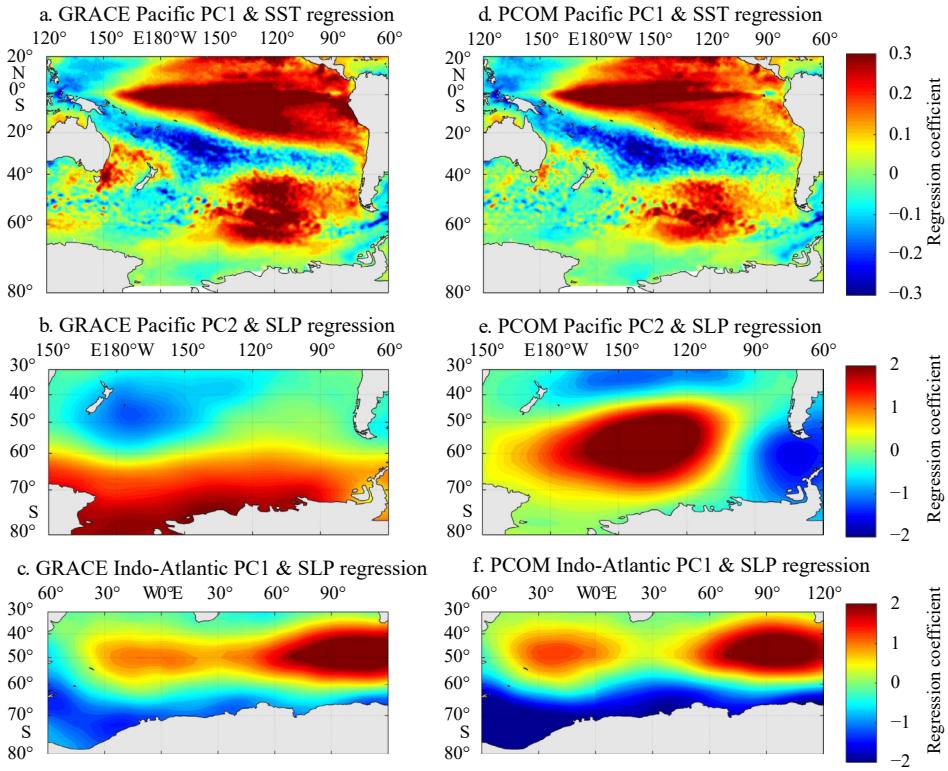

Fig. 9. SST (unit: °C) pattern regressed onto PC1 time series (upper panels) and SLP (unit: hPa) pattern regressed onto PC2 time series (middle panels) in the South Pacific Ocean, and SLP pattern regressed onto PC1 time series of OBP anomaly in the South Indo-Atlantic Ocean (lower panels); OBP based on GRACE (left panels) and PCOM (right panels). The anomalies are calculated by subtracting climatological annual cycle.

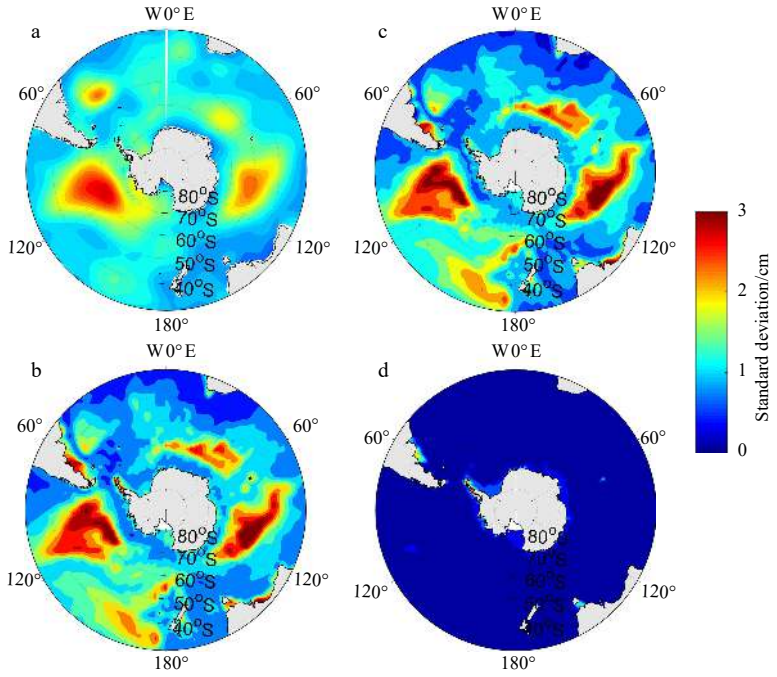

Fig. 10. Standard deviation of interannual GRACE OBP (in unit of cm) in the Southern Ocean (a), standard deviation of interannual OBP in the Southern Ocean from control run of PCOM (Exp. 1) (b), standard deviation of interannual OBP in the Southern Ocean from control run of PCOM (Exp. 2) (c), and standard deviation of interannual OBP in the Southern Ocean from control run of PCOM (Exp. 3) (d) from 2003 to 2016.

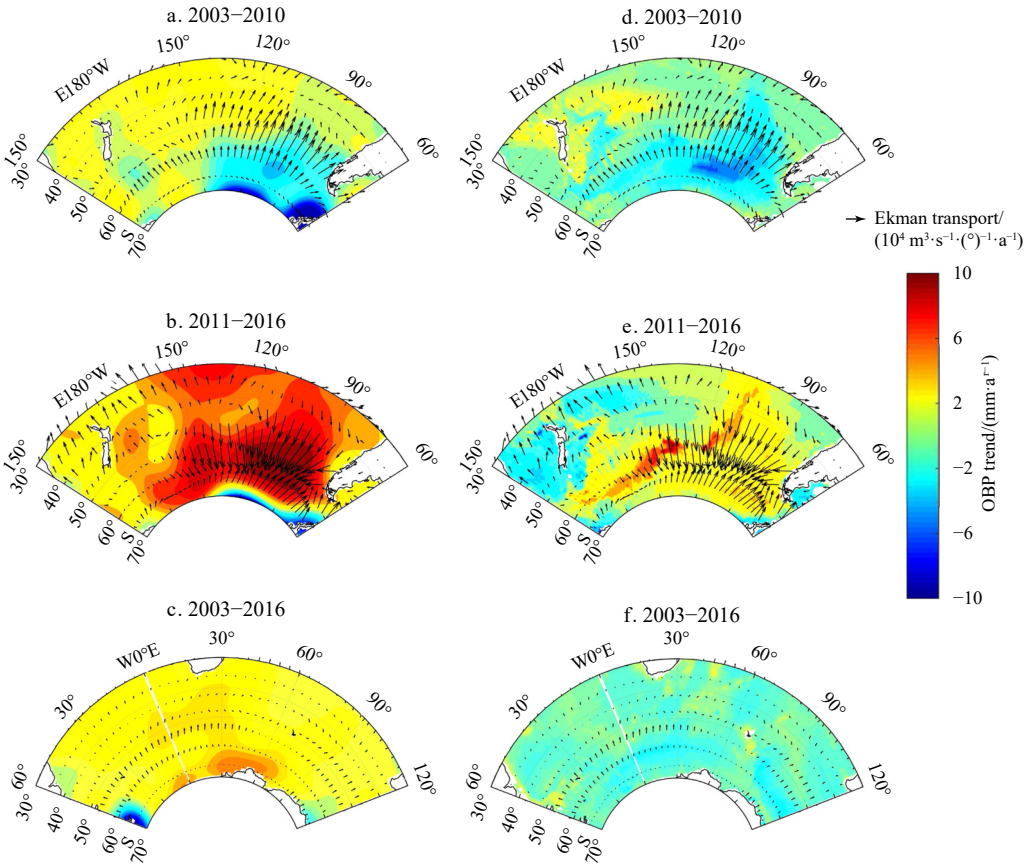

Fig. 11. Trends of OBP (color shading, mm/a) and Ekman transport (vector, m^3/(°)) based on Grace (left panels) and PCOM (right panels). a, b, d and e. For the two periods of 2003–2010 (a, d) and 2011–2016 (b, e) in the South Pacific Ocean; c and f. for the period of 2003–2016 in the South Indo-Atlantic Ocean.

pact of wind fields. By comparing steric sea level, OBP and the sea level anomalies from 2003 to 2016, it is found that the steric sea level and the total sea level distribution are well-correlated to each other at mid-latitudes in the Southern Ocean. In contrast, the OBP variability dominates the sea level variability at seasonal and interannual time scales at high latitudes. The reconstructed OBP based on barotropic vorticity equation has a good correlation with the observations, not only at the annual cycle but also at interannual timescales. Thus, wind forcing plays an important role in the variability of the OBP in the Southern Ocean.

At interannual timescales, ENSO and SAM have significant impacts on the OBP variability in the southern Pacific and southern Indian Ocean. The leading patterns of OBP correspond well to Ekman transport associated with ENSO and SAM. The pattern of the leading EOF modes of PCOM OBP are very similar to the observed OBP, with a significant correlation coefficient at 0.78 (significant at a 99% confidence level). Sensitive experiments of PCOM show that surface wind forcing accounts for the overwhelming part of the observed OBP variability, while the SLP forcing can be ignored at seasonal and interannual timescales.

Although PCOM can reproduce seasonal and interannual OBP changes quite well in the Southern Ocean, the model needs further improvements. In particular, the effects of glaciers and rivers should be included, such improvements can enhance model performance in simulating the impacts of global warming on the regional OBP and sea level change. Currently, the timeseries of GRACE satellite data is not long enough for the decadal analysis. Given the important role of OBP in sea level change, longer time series of observational data are crucial for exploring OBP mechanisms and predicting sea level change.

References

Androsov A, Boebel O, Schröter J, et al. 2020. Ocean bottom pressure variability: Can it be reliably modeled?. Journal of Geophysical Research: Oceans, 125(3): e2019JC015469

Antonov J I, Seidov D, Boyer T P, et al. 2010. World Ocean Atlas 2009, Volume 2: Salinity. NOAA Atlas NESDIS 69. Washington, DC: U S Government Printing Office

Bergmann I, Dobslaw H. 2012. Short-term transport variability of the Antarctic Circumpolar Current from satellite gravity observations. Journal of Geophysical Research: Oceans, 117(C5): C05044

Boening C, Lee T, Zlotnicki V. 2011. A record-high ocean bottom pressure in the South Pacific observed by GRACE. Geophysical Research Letters, 38(4): L04602

Boening C, Willis J K, Landerer F W, et al. 2012. The 2011 La Niña: So strong, the oceans fell. Geophysical Research Letters, 39(19): L19602

Brunnabend S E, Rietbroek R, Timmermann R, et al. 2011. Improving mass redistribution estimates by modeling ocean bottom pressure uncertainties. Journal of Geophysical Research: Oceans, 116(C8): C08037

Cabanes C, Huck T, De Verdière A C. 2006. Contributions of wind forcing and surface heating to interannual sea level variations in the Atlantic Ocean. Journal of Physical Oceanography, 36(9): 1739–1750, doi: 10.1175/JPO2935.1

Cazenave A, Dieng H B, Meyssignac B, et al. 2014. The rate of sea-level rise. Nature Climate Change, 4(5): 358–361, doi: 10.1038/nclimate2159

Cazenave A, Henry O, Munier S, et al. 2012. Estimating ENSO influence on the global mean sea level, 1993–2010. Marine Geodesy, 35(S1): 82–97

Chambers D P, Cazenave A, Champollion N, et al. 2017. Evaluation of the global mean sea level budget between 1993 and 2014. Surveys in Geophysics, 38(1): 309–327, doi: 10.1007/s10712-016-9381-3

Cheng Xuhua, Li Lijuan, Du Yan, et al. 2013. Mass-induced sea level change in the northwestern North Pacific and its contribution to total sea level change. Geophysical Research Letters, 40(15): 3975–3980, doi: 10.1002/grl.50748

Dukowicz J K. 1997. Steric sea level in the los alamos POP code—non-boussinesq effects. Atmosphere-Ocean, 35(S1): 533–546

Fasullo J T, Boening C, Landerer F W, et al. 2013. Australia's unique influence on global sea level in 2010–2011. Geophysical Research Letters, 40(16): 4368–4373, doi: 10.1002/grl.50834

Gill A E, Niller P P. 1973. The theory of the seasonal variability in the ocean. Deep Sea Research and Oceanographic Abstracts, 20(2): 141–177, doi: 10.1016/0011-7471(73)90049-1

Greatbatch R J. 1994. A note on the representation of steric sea level in models that conserve volume rather than mass. Journal of Geophysical Research: Oceans, 99(C6): 12767–12771, doi: 10.1029/94JC00847

Henley B J, Gergis J, Karoly D J, et al. 2015. A tripole index for the interdecadal Pacific oscillation. Climate Dynamics, 45(11/12): 3077–3090, doi: 10.1007/s00382-015-2525-1

Huang Ruixin, Jin Xiangze, Zhang Xuehong. 2001. An oceanic general circulation model in pressure coordinates. Advances in Atmospheric Sciences, 18(1): 1–22, doi: 10.1007/s00376-001-0001-9

Johnson G C, Chambers D P. 2013. Ocean bottom pressure seasonal cycles and decadal trends from GRACE Release-05: Ocean circulation implications. Journal of Geophysical Research: Oceans, 118(9): 4228–4240, doi: 10.1002/jgrc.20307

Kalnay E, Kanamitsu M, Kistler R, et al. 1996. The NCEP/NCAR 40-year reanalysis project. Bulletin of the American Meteorological Society, 77(3): 437–472, doi: 10.1175/1520-0477(1996)077<0437:TNYRP>2.0.CO;2

Li Hong, Xu Fanghua, Zhou Wei, et al. 2017. Development of a global gridded Argo data set with Barnes successive corrections. Journal of Geophysical Research: Oceans, 122(2): 866–889, doi: 10.1002/2016JC012285

Liau J R, Chao B F. 2017. Variation of Antarctic circumpolar current and its intensification in relation to the southern annular mode detected in the time-variable gravity signals by GRACE satellite. Earth, Planets and Space, 69: 93

Locarnini R A, Mishonov A V, Antonov J I, et al. 2010. World Ocean Atlas 2009, Volume 1: Temperature. NOAA Atlas NESDIS 68. Washington, DC: U S Government Printing Office

Makowski J K, Chambers D P, Bonin J A. 2015. Using ocean bottom pressure from the gravity recovery and climate experiment (GRACE) to estimate transport variability in the southern Indian Ocean. Journal of Geophysical Research: Oceans, 120(6): 4245–4259, doi: 10.1002/2014JC010575

Marshall G J. 2003. Trends in the southern annular mode from observations and reanalyses. Journal of Climate, 16(24): 4134–4143, doi: 10.1175/1520-0442(2003)016<4134:TITSAM>2.0.CO;2

Meredith M P, Woodworth P L, Chereskin T K, et al. 2011. Sustained monitoring of the southern ocean at drake passage: Past achievements and future priorities. Reviews of Geophysics, 49(4): RG4005

Ou Niansen, Lin Yihua, Bi Xunqiang, et al. 2016. Baseline evaluation of a pressure coordinate ocean model (PCOM 1.0). Climatic and Environmental Research, 21(1): 56–64

Peralta-Ferriz C, Landerer F W, Chambers D, et al. 2017. Remote sensing of bottom pressure from GRACE satellites. US CLIVAR Variations Newsletter, 15(2): 22–28

Piecuch C G, Quinn K J, Ponte R M. 2013. Satellite-derived interannual ocean bottom pressure variability and its relation to sea level. Geophysical Research Letters, 40(12): 3106–3110, doi: 10.1002/grl.50549

Ponte R M. 1999. A preliminary model study of the large-scale seasonal cycle in bottom pressure over the global ocean. Journal of Geophysical Research: Oceans, 104(C1): 1289–1300, doi: 10.1029/1998JC900028

Ponte R M, Piecuch C G. 2014. Interannual bottom pressure signals in the Australian–Antarctic and Bellingshausen basins. Journal of Physical Oceanography, 44(5): 1456–1465, doi: 10.1175/JPO-D-13-0223.1

Quinn K J, Ponte R M. 2012. High frequency barotropic ocean variability observed by GRACE and satellite altimetry. Geophysical Research Letters, 39(7): L07603

Song Y T, Zlotnicki V. 2008. Subpolar ocean bottom pressure oscillation and its links to the tropical ENSO. International Journal of Remote Sensing, 29(21): 6091–6107, doi: 10.1080/01431160

802175538

Stammer D, Tokmakian R, Semtner A, et al. 1996. How well does a 1/4° global circulation model simulate large-scale oceanic observations?. Journal of Geophysical Research: Oceans, 101(C11): 25779–25811

Stepanov V N, Hughes C W. 2006. Propagation of signals in basin-scale ocean bottom pressure from a barotropic model. Journal of Geophysical Research: Oceans, 111(C12): C12002, doi: 10.1029/2005JC003450

Thomson R E, Tabata S. 1989. Steric sea level trends in the Northeast Pacific Ocean: Possible evidence of global sea level rise. Journal of Climate, 2(6): 542–553, doi: 10.1175/1520-0442(1989)002<0542:SSLTIT>2.0.CO;2

Vivier F, Kelly K A, Harismendy M. 2005. Causes of large-scale sea level variations in the Southern Ocean: Analyses of sea level and a barotropic model. Journal of Geophysical Research: Oceans, 110(C9): C09014

Wang Juan, Wang Jing, Cheng Xuhua. 2015. Mass-induced sea level variations in the Gulf of Carpentaria. Journal of Oceanography, 71(4): 449–461, doi: 10.1007/s10872-015-0304-6

Zhang Yu, Lin Yihua, Huang Ruixin. 2014. A climatic dataset of ocean vertical turbulent mixing coefficient based on real energy sources. Science China Earth Sciences, 57(10): 2435–2446, doi: 10.1007/s11430-014-4904-6

Zlotnicki V, Wahr J, Fukumori I, et al. 2007. Antarctic circumpolar current transport variability during 2003–05 from GRACE. Journal of Physical Oceanography, 37(2): 230–244, doi: 10.1175/JPO3009.1